DEFORMATION and RUPTURE of the OCEANIC CRUST MAY CONTROL GROWTH of HAWAIIAN VOLCANOES

Jean-Luc Got, Vadim Monteiller, Julien Monteux, Riad Hassani, Paul Okubo

DEFORMATION and RUPTURE
of the OCEANIC CRUST MAY CONTROL
GROWTH of HAWAIIAN VOLCANOES

Jean-Luc Got[1], Vadim Monteiller[1], Julien Monteux[2], Riad Hassani[1], Paul Okubo[3]

(1) Laboratoire de Géophysique Interne et Tectonophysique, Université de Savoie, 73376, Le Bourget-du-Lac, France.

(2) Laboratoire de Sciences de la Terre, Ecole Normale Supérieure, 69364, Lyon, France.

(3) USGS – Hawaiian Volcano Observatory, Hawaii National Park, 97560, Hawaii.

The double-difference location of similar earthquakes in a heterogeneous velocity model, and the constraints provided by tomography and mechanical modeling show that the load exerted by large Hawaiian volcanoes can be sufficient to rupture oceanic crust. In turn, this intense deformation controls the surface morphology of the volcanoes: rift zones, topographic slopes and flank instabilities.

Hawaiian volcanoes are formed by the emission of large quantities of basaltic magma related to hot-spot activity below the Pacific Plate. Despite the apparent simplicity of the parent-process – simple emission of magma onto the oceanic crust (OC) – the resulting edifices display some topographic complexity. Nevertheless, certain features, such as rift zones and large flank slides, are common to all Hawaiian volcanoes, indicating profound similarities in their genesis. In order to understand this morphology, we need to combine information about the deep structure of the volcanoes, provided by accumulating geophysical data, with studies of the mechanical interactions that take place within the edifices and within the OC.

In this work, we first computed a 3D P-wave velocity model of Mauna Loa Volcano (ML) and Kilauea Volcano (KV), using data from 1435 earthquakes that were well recorded (>= 25 stations) by the HVO network between 1988 and 1999. These events were declustered in such a way that the earthquake-station ray set optimally sampled the tomographic volume. The 44,504 high-quality P arrival-times were inverted using Monteiller's probabilistic algorithm (1). The resulting 3D velocity model (959,077 1-km^3 cubic cells) was stable and detailed, and showed most of the volcanoes' structural features (Figure 1). Therefore, we used this model to compute double-difference locations for 1161 correlated earthquakes in the south flank of KV recorded between 1988 and 1999 by the HVO seismic network (Figure 2a). The quality of the velocity model ensured that the slowness vectors used in the double-difference locations were correctly computed. To illustrate the coherence between time delays, earthquake locations and the slowness vectors, we plotted time delays as a function of the angle between the slowness vector and the relative position vector for each coherent earthquake pair and each station (Figure 2b). The accurate sinusoidal pattern revealed by this plot showed that the derived locations were almost perfectly coherent with the slowness vectors computed using the tomographic model: the error in the estimation of the direction of each earthquake doublet was less than 5°. The double difference location results showed earthquake locations on the subhorizontal decollement plane found by Got et al. (4), and along a deeper, steeper, southward-dipping reverse fault; thus, confirming some preliminary results obtained by Got and Okubo (5) using a 1-D model. The depth inferred for the decollement plane (8-9km) was obtained by double-difference relocation using time-delay measurements computed from widely correlated events into the 3D

2

velocity model. Coherence remained greater than 80% for inter-event distances up to 1km, leading to a well-conditioned inversion. This provides an accuracy of better than 500m for the earthquake depth calculations. The 8.5-km depth coincides locally with the top of the OC (6-7).

Travel-time tomography was used to determine the deep structure of the volcanoes. The resulting cross-sections show roughly triangular, high-velocity cores beneath the calderas and rifts. Plots of P-wave velocities in the south flank of KV along a N-S horizontal profile (Figure 2c) showed that velocity falls substantially with distance from the rift axis. Strikingly, the norm of the velocity gradient is largest near the intersection of the reverse fault plane and the decollement plane. This maximum is reached for a ~6 km/**s** P-wave velocity, which is the limit used (6) to differentiate between intrusive rocks and lava flows in Hawaiian volcanoes. Hence, an accurate analysis of seismological data tends to show that reverse faulting occurs in the south flank of KV. It initiates near the core/cover boundary, at the depth of the decollement plane, and propagates through the oceanic crust.

In order to ascertain the conditions required for such a rupture of the OC to take place, this indirect observation must be combined with mechanics. Therefore we drew up a mechanical model of the interaction between Hawaiian-type volcanoes and OC. Geometrical boundary conditions and constitutive laws of these bodies are provided by tomographic results and Hill and Zucca's (6) correspondence between local rock formations and velocities. Drilling experiments (8) in and around rift zones have reached depths of up to 3km. They have shown that the peripheral cover surrounding rift zones is

mainly composed of altered lavas whose mechanical properties are characterized by low Young's modulus, cohesion and friction coefficient. We therefore represented the slow peripheral cover by an elastic-plastic material (E = 30 GPa, ν = 0.25, C = 1 MPa, ϕ = 10° to 20°, ρ = 2600 kg/m^3), whereas the measured seismic velocities indicated an elastic material for the dense and fast cores (E = 100 GPa, ν = 0.25, ρ = 2900 kg/m^3). The OC was represented by an elastic-plastic material (E = 100 GPa, ν = 0.25, C = 1 MPa, ϕ = 15°, ρ = 2900 kg/m^3). Basal decollement (top of the OC) is represented by an interface with a Coulomb friction law (ϕ = 10°; 9-10). Finite-element calculations of the deformation of this model were carried out using the ADELI code (11). These calculations (Figure 3) show that, providing there is a realistic density and rheological contrast between the core and the cover, the deviatoric stress can locally attain the plasticity threshold and reverse faults can cut through the OC. Thus, the load of the volcano can cause intense plastic deformation of the OC, even though the volcano may be of relatively limited size, as is the case for KV. If the volcano is sufficiently large, as is the case for ML, the oceanic crust may rupture completely. This model also shows that the effusive cover, both between ML and KV, and on the south flank of KV, is plasticized by the squeezing action of the dense and rigid cores of the volcanoes. The location of this deformation is clearly controlled by the spatial distribution of rheologies and densities. Plastified zones correspond to the Hilina fault scarps in the south flank of KV and to the Kaoiki fault zone in the SE flank of ML. This deformation is due to the action of gravity and the interaction of the volcanic bodies with the (flexured) OC. The correlation observed between displacement, seismicity, and

4

intrusions-eruptions in the south flank of KV (12) specifically shows that the volcanic edifice is close to the critical state.

Double-difference relocation of 732 earthquakes (Figure 4a) indicated that decollement earthquakes occur at depths of around 10 to 11km under ML and at depths of around 8 to 9km under the south flank of KV. The vertical uncertainty for these relocations was less than 500m. The difference in decollement depth is about 2 +/- 1km for 10 to 15km horizontally between ML and KV. Based on the hypothesis that the decollement plane coincides with the top of the OC, the top of the OC between KV and ML slopes at an angle of 9° +/- 5°, whereas the average slope below the OC of the Hawaiian islands is between 1.5 and 3°. This has been confirmed by careful inspection of active seismic results (*e.g.* 6, 7, Fig. 15). Such local variations in flexure may be considered anomalous and they cannot be explained using homogeneous elastic models (15). Elastic-plastic models (Figure 3a) also place the bases of ML and KV at similar levels. If such a slope variation was confined to the 5- to 6-km thick crust, it would represent an unrealistic deformation of 20 to 40%; hence this deformation must also concern the upper mantle. Interestingly, the SW rift zone occupies the same position with respect to ML as the reverse fault evidenced by double-difference location occupies with respect to KV. These observations and the results of elastic-plastic modeling on the scale of ML (Figure 3b) suggest that the rift system forming KV may have originated in the rupturing of the OC caused by the load exerted by ML, leading to local collapse of the OC below ML. Thus, the initiation and development of a rift system in Hawaiian volcanoes might be a step in the collapse of the structure caused by its own mass, eventually accelerated by a decrease in magmatic pressure as the Pacific Plate

moves above the mantle plume. Wolfe (16) showed that the deeper seismicity (~30km) in the neighborhood of the ML-KV feeding system is of tectonic origin and organized in sub-horizontal planes. This indicates that deep movements exist and that they are linked to the feeding system; sub-horizontal movements may be compatible with collapse. Vertical growth of the volcano, rupture of the OC, simultaneous collapse and creation of rift zones constitute a growth model for Hawaiian volcanoes on the surface of the Pacific Plate.

As Hawaiian volcanoes deform the underlying OC (mostly vertically), topographic variations in the top of the OC may constrain the (horizontal) growth of Hawaiian volcanoes. In fact, geodetic measurements clearly show that KV, and to a lesser extent ML, grow horizontally (*e.g.*, 12, 17-20). It is often thought that KV buttresses ML, blocking its seaward displacement. The topography of the OC may provide a more efficient explanation. The tangential force, F, required to move a non-deformable wedge of weight P, along a slope inclined at an angle θ, and with an internal angle of friction ϕ is

$$F = P \, tg(\theta+\phi)$$

The apparent basal friction coefficient along the decollement plane of KV is thought to be very low (close to 0.1; i.e. $\phi \sim 5$ to $10°$; 7-8). With such friction coefficients, more than three times as much energy is required to move a body up a $10°$ slope than along a horizontal surface. To reach an equivalent value by increasing the weight, P, of the wedge, the thickness of KV would have to be double the thickness of the SE flank of ML, which is contrary to the best recent estimates (21). Therefore, an increase in the slope of the top of the OC is a highly plausible mechanism for the buttressing of the SE flank of ML. If we

accept the hypothesis of a low basal friction coefficient ϕ combined with a "small" KV, the slope of the interface (top of the OC) will be a critical factor in determining the mechanical evolution of ML and KV. The low ϕ does not damp the influence of the variations of the topography of the OC; it explains why the surface topographic slopes are steeper near large eruptive centers, such as ML (22). The apparent coefficient of friction increases with the slope of the OC and the edifice remains stable for higher topographic slopes, as long as it has sufficient internal strength (*e.g.*, 7-8). The variations in the slope of the OC across and along the rift zones may explain the topographical readjustments observed (e.g. Hilina Pali-type giant escarpments, see 23-25; 4-5; 10).

The topography of the OC may be responsible for two other major characteristics of the seismo-mechanical activity in this region: (1) the blocking and relative weak eruptive activity along the SW rift zone, whereas the east rift zone is very active; (2) the existence of an "aseismic" zone (from a micro-seismicity point of view) along the ramp, whereas ML continues to show a certain amount of activity, notably due to inflations (20). Could this zone accumulate sufficient stress to be the source of major earthquakes, such as the great Kau (M~8) earthquake? If this is the case, these major earthquakes provide a mechanism for Lipman's "piggyback" tectonics (21) under today's conditions.

REFERENCES

[1] Monteiller, V., Got, J.-L., Virieux, J. and P.G. Okubo, 2005, An efficient algorithm for double-difference tomography and location in heterogeneous media, with an application to the Kilauea volcano, Hawaii, *J. Geophys. Res.,* **110**, B12306, doi:10.1029/2004JB003466**.**

[2] Thurber, C.H., 1984, Seismic detection of the summit magma complex of Kilauea Volcano, Hawaii, *Science*, **223**, 165-167.

[3] Okubo, P., H.M. Benz, and B.A. Chouet, Imaging the crustal magma sources beneath Mauna Loa and Kilauea volcanoes, Hawaii, *Geology*, **25**, 867-870, 1997.

[4] Got, J.-L., J. Fréchet, and F.W. Klein, 1994, Deep fault plane geometry inferred from multiplet relative relocation beneath the south flank of Kilauea, *J. Geophys. Res.,* **99***, 15375-15386, 1994.*

[5] Got, J.-L., and P. G. Okubo, 2003, New insights into Kilauea's volcano dynamics brought by large-scale relative relocation of microearthquakes*, J. Geophys. Res.,* **108***, 2337, doi :10.1029/2002JB002060.

[6] Hill, D.P., and J.J. Zucca, 1987, Geophysical constraints on the structure of Kilauea and Mauna Loa volcanoes and some implications for seismomagmatic processes, in Decker, R.W., Wright, T.L., Stauffer, P.H., Eds, *U.S. Geol. Surv. Prof. Pap.*, **1350**, vol. 2, 903-917.

[7] Watts, A.B. and U.S. ten Brink, 1989, Crustal structure, flexure and subsidence history of the Hawaiian islands, *J. Geophys. Res.,* **94***, 10473-10500.

[8] Schiffman, P., Watters, R.J., Thompson, N., and A.W. Walton, 2006, Hyaloclastites and the slope stability of Hawaiian volcanoes: insights from the Hawaiian Scientific Drilling

Project's 3-km drill core, *J. Volcanol. Geotherm. Res.*, **150**, doi:10.1016/j.jvolgeores.2005.07.030.

[9] Dieterich, J.H., 1988, Growth and persistence of Hawaiian volcanic rift zones, *J. Geophys. Res.*, **93**, 4258-4270.

[10] Morgan, J.K., 2006, Volcanotectonic interactions between Mauna Loa and Kilauea: insights from 2-D discrete element simulations, *J. Volcanol. Geotherm. Res.*, **150**, doi:10.1016/j.jvolgeores.2005.07.025.

[11] Hassani, R. and J. Chéry, 1996, Anelasticity explains topography associated with Basin and Range normal faulting. *Geology*, **24**, 12, 1095-1098.

[12] Swanson, D. A., W. A. Duffield, and R. S. Fiske, 1976, Displacement of the south flank of Kilauea volcano : The result of forceful intrusion of magma into the rift zones, *U. S. Geol. Surv. Prof. Pap., 963*, 1-39.

[13] Denlinger R.P., and P.G. Okubo, 1995, Structure of the mobile south flank of Kilauea Volcano, Hawaii, *J. Geophys. Res.*, **100**, 24499-24507.

[14] Klein, F.W., Koyanagi, R.Y., Nakata, J.S., and W.R. Tanigawa, 1987, The seismicity of Kilauea's magma system, in Decker, R.W., Wright, T.L., Stauffer, P.H., Eds, *U.S. Geol. Surv. Prof. Pap.*, **1350**, vol. 2, 1019-1186.

[15] Wessel, P., 1993, A re-examination of the flexural deformation beneath the Hawaiian islands, *J. Geophys. Res., 98,* 12177-12190.

[16] Wolfe, C., Okubo, P.G., and P. Shearer, 2003, Mantle fault zone beneath Kilauea volcano, Hawaii, *Science*, **300**, 478-480.

[17] Delaney, P.T., Fiske, R.S., Miklius, A., Okamura, A.T., and M.K. Sako, 1990, Deep magma body beneath the summit and rift zones of Kilauea volcano, Hawaii, *Science*, **247**, 1311-1316.

[18] Owen, S., Segall, P., Lisowski, M., Miklius, A., Denlinger, R., and M. Sako, 1995, Rapid deformation of the south flank of Kilauea volcano, Hawai'i, *Science*, **267**, 1328-1332.

[19] Cervelli, P., Segall, P., Johnson, K., Lisowski, and A. Miklius, 2002, Sudden aseismic fault slip on the south flank of Kilauea volcano, *Nature*, **415**, 1014-1018.

[20] Miklius and Cervelli, 2003, Interaction between Kilauea and Mauna Loa, *Nature*, **421**, 229-230.

[21] Lipman, P.W., Sisson, T.W., Coombs, M.L., Calvert, A., Kimura, J.-I., 2006, Piggyback tectonics: long-term growth of Kilauea on the south flank of Mauna Loa, *J. Volcanol. Geotherm. Res.*, **150**, doi:10.1016/j.jvolgeores.2005.07.032.

[22] Mark, R.K., and J.G. Moore, 1987, Slopes of the Hawaiian ridge, in Decker, R.W., Wright, T.L., Stauffer, P.H., Eds, *U.S. Geol. Surv. Prof. Pap.*, **1350**, vol. 1, 101-107.

[23] Lipman, P.W., Normark, W.R., Moore, J.G., Wilson, J.B., and C.E. Gutmacher, 1988, The giant submarine Alika debris slide, Mauna Loa, Hawaii, *J. Geophys. Res.,* **93**, 4279-4299.

[24] Moore, J.G., Clague, D.A., Holcomb, R.T., Lipman, P.W., Normark, W.R., and M.E. Torresan, 1989, Prodigious submarine landslides on the Hawaiian ridge, *J. Geophys. Res.,* **94**, 17465-17484.

[25] Moore, J.G., Normark, W.R., and R.T Holcomb, 1994, Giant Hawaiian landslides, *Annu. Rev. Earth Planet. Sci.*, **22**, 119-144.

FIGURE CAPTIONS:

Figure 1: Map of Hawaii Island showing the main topographic features, the epicenters of the earthquakes used for the tomographic model (white dots), for the double difference relocation (black dots) and the location of the HVO short-period seismic stations (open triangles). The solid rectangle and the solid line show the locations of the cross-sections presented respectively in Figures 2 (a) and (c) and in Figure 4. Color is used to represent P-wave seismic velocities after travel-time tomographic inversion, at 6-km depth. The resulting model is the simplest that best fits the data (optimal *a priori* information: velocity parameter correlation length λ = 5km, velocity standard deviation σ_v = 1 km/s). See also (2-3).

Figure 2: **(a)** N-S cross-section of the velocity model (Figure 1) and location of relocated earthquakes on the south flank of KV. The color scale highlights the 5.8 – 6.2 km/s velocity interval that marks the separation between intrusive rocks and lava flows, according to (6), Figure 37.2. Double-difference relocation uses this tomographic velocity model, thereby ensuring that ray parameters are correctly calculated. Relocation was carried out using 1161 correlated earthquakes (coherence > 80%) on the south flank of KV recorded by the HVO network between 1988 and 1999. The average errors for the relocations were found to be 100m vertically and 50m horizontally.

(b) Time delay as a function of the angle between the wave vector at the hypocenter and the relative position vector for each earthquake pair. The delays were computed for 90% coherent seismic signals recorded by each seismic station in the HVO network for each pair of similar earthquakes belonging to the 1161 earthquakes used for the relocation. The color scale shows the frequency of appearance of time delay values. A sinusoidal form was obtained, showing the coherence of the solution (positions) with the slowness vectors (velocity model).

(c) Velocity (solid line) and velocity gradient (dashed line) as a function of distance along a horizontal N-S profile across the south flank of Kilauea. The velocity profile is the mean, at 8.5 km depth, of ten N-S contiguous profiles across the rectangular area indicated in Figure 1. The arrow indicates the abscissa of the intersection of the reverse fault with the decollement plane; it shows that the reverse fault initiates in the neighborhood of the highest velocity gradient.

Figure 3: **(a)** Model of the interaction between the volcanic edifice and the OC, produced using the ADELI code (11). The ML and KV volcanoes are represented each by a dense and elastic core of intrusive origin, and a light elastic-plastic cover. The OC is represented by an elastic-plastic material. The dimensions of the dense and rigid cores were deduced from the tomographic model. Colors are used to show the plastic deformation (norm of the deviatoric plastic strain tensor).

(b) Model of the squeezing of the elastic-plastic OC by an isolated volcano the size of ML. A reverse fault, which cuts through the entire OC, is created at the edge of the dense and

rigid core. It has an identical dip to the fault found by double-difference relocation (Figure 2a).

Figure 4: **(a)** E-W cross-section between ML and the south flank of KV (see earthquake locations and profile A-A', Figure 1) showing the tomographic model and relocated earthquakes. Resolution of the tomographic model is represented through a checkerboard test (Figure 4b). 732 relocated earthquakes along the decollement plane beneath ML and the south flank of KV were identified using a cross-spectral coherence criterion (similarity of the waveforms), and relocated using cross-spectral time delays. Events located beneath the easternmost part of the SE flank of ML (longitude: 62 to 72km) were selected for the similarity of their travel-times and focal mechanisms, and relocated using travel-time differences. See also (13), Figure 5 and (14).

(b) Result of a checkerboard test along the same cross-section as Figure 4a, showing the earthquakes used to compute the tomographic model. Travel times were computed for the same earthquake-station set as in Figure 4a, using a 1% sinusoidal velocity perturbation (wavelength: 10km horizontally, 2km vertically) of the P-wave velocity model. The propagation medium is well-reconstructed in most of the volume of interest.

Supporting On-line Material

Figure SOM1: Model of the interaction between the volcanic edifice and the OC, produced using the ADELI code (11). The ML and KV volcanoes are represented each by a dense and elastic core of intrusive origin, and a light elastic-plastic cover. The OC is represented by an elastic-plastic material. The dimensions of the dense and rigid cores were deduced from the tomographic model. Colors are used to show the plastic deformation (norm of the deviatoric plastic strain tensor). Vectors show the principal (deviatoric) stresses. The peripheral cover undergoes horizontal compression between ML and KV (due to the flexure of the OC), and horizontal tension in the south flank of KV (due to the gravitational stresses and the low frictional coefficients, $\phi = 10°$ and $\phi = 15°$, used respectively for modeling the subhorizontal decollement plane and the elastic-plastic cover).

Figure SOM2: Same as Figure SOM1, showing the principal deviatoric stresses in the elastice cores, in the oceanic crust and in the upper mantle.
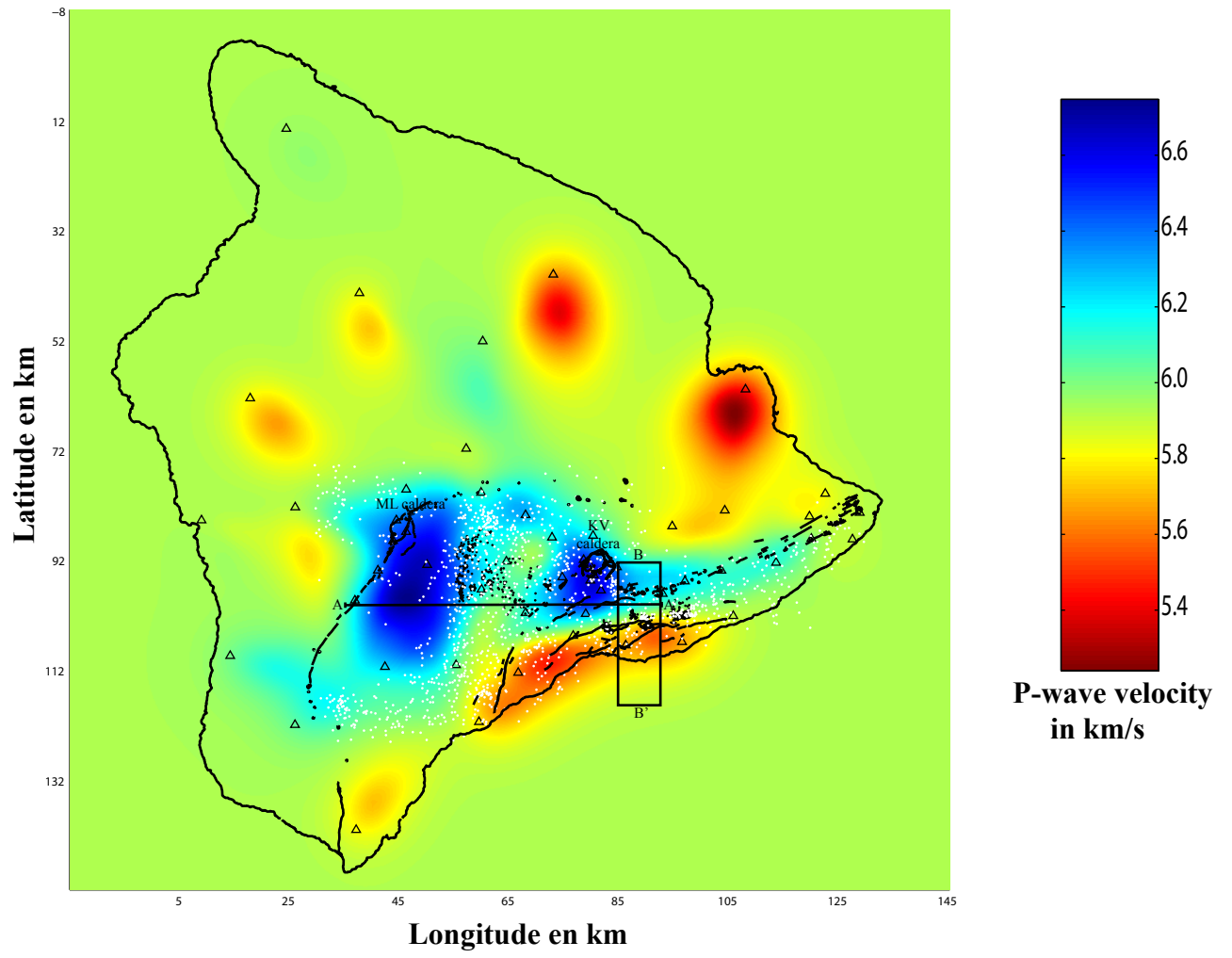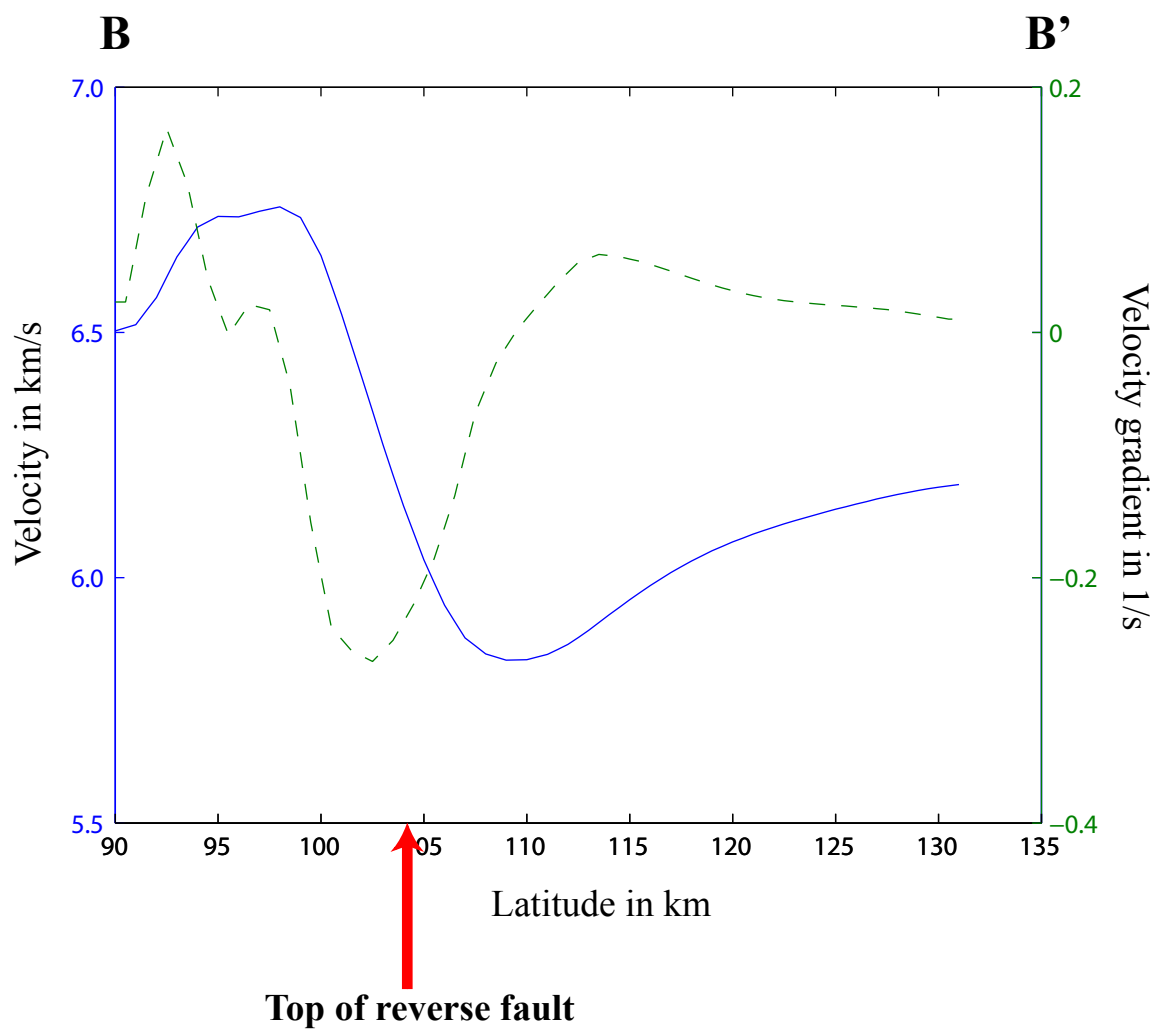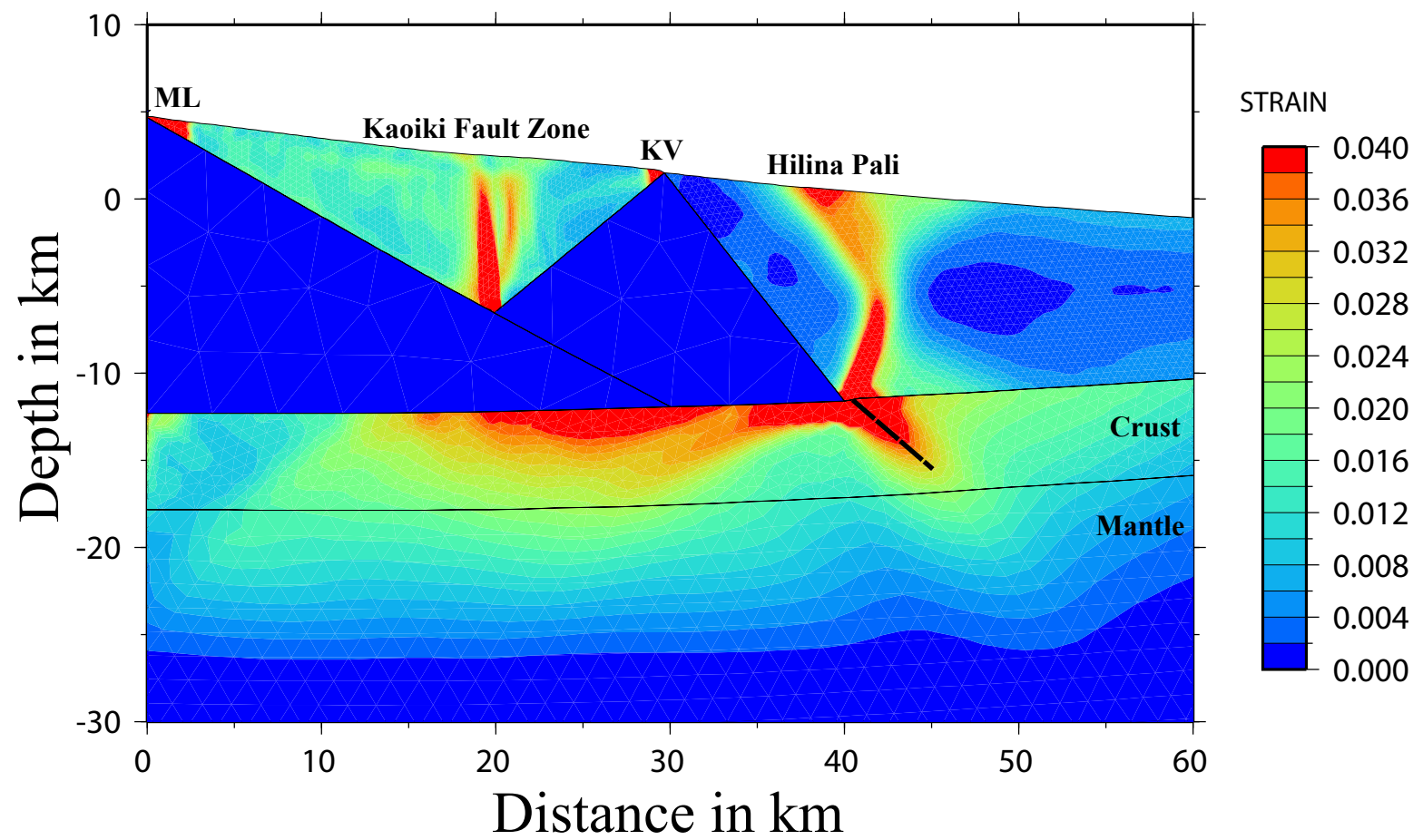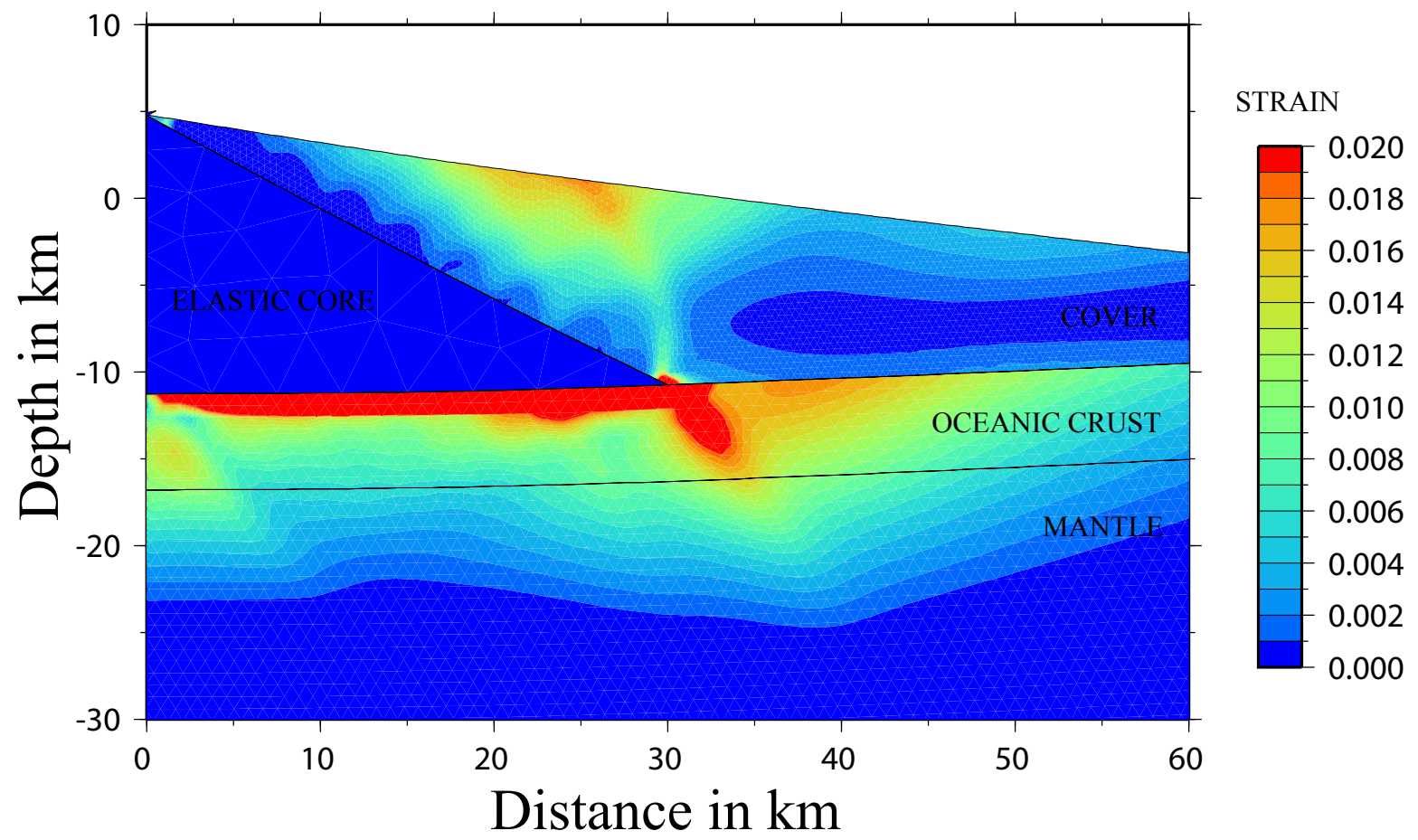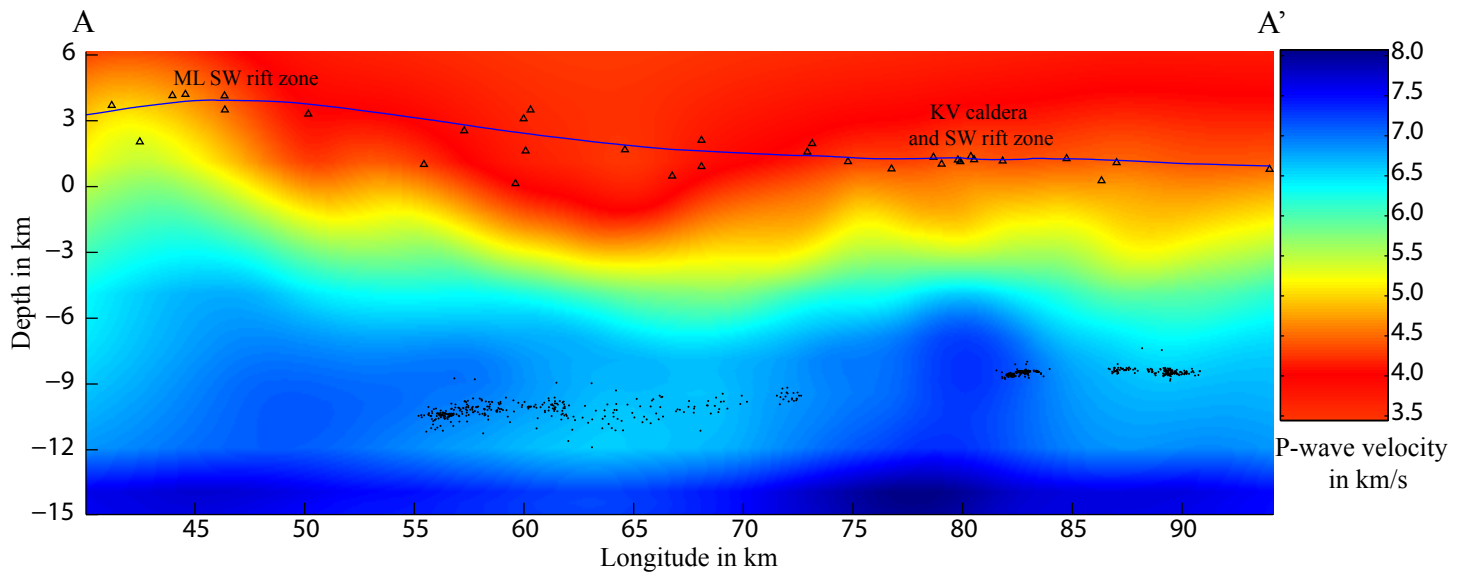
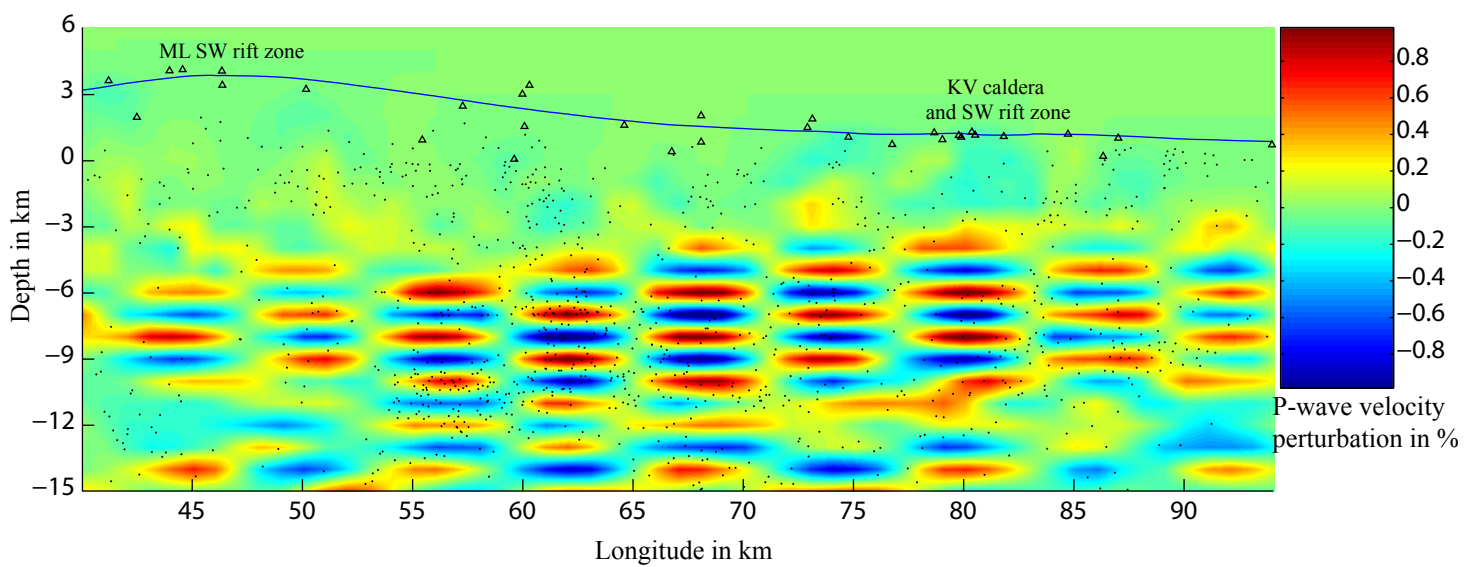Figure 1
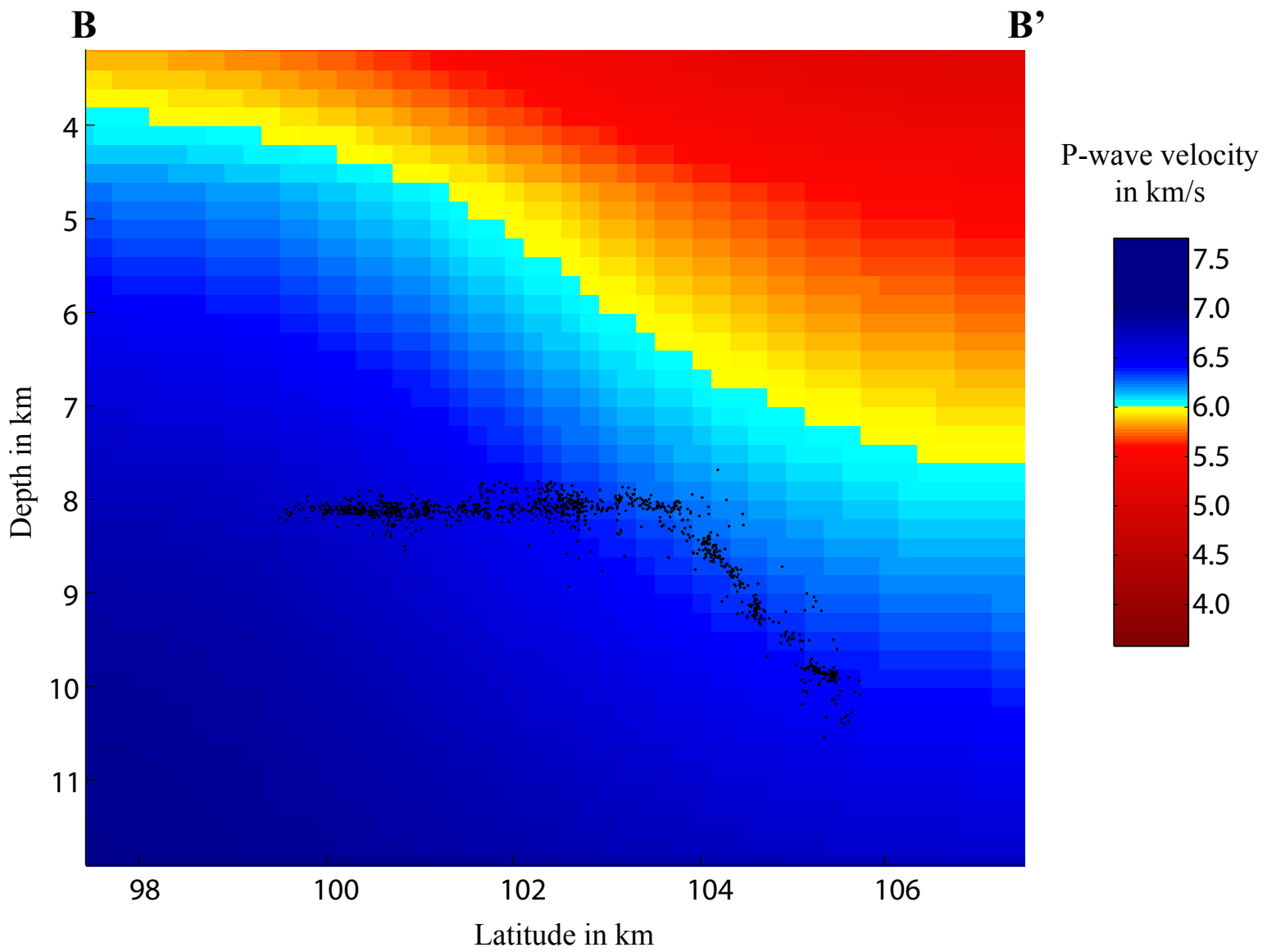
Figure 2a
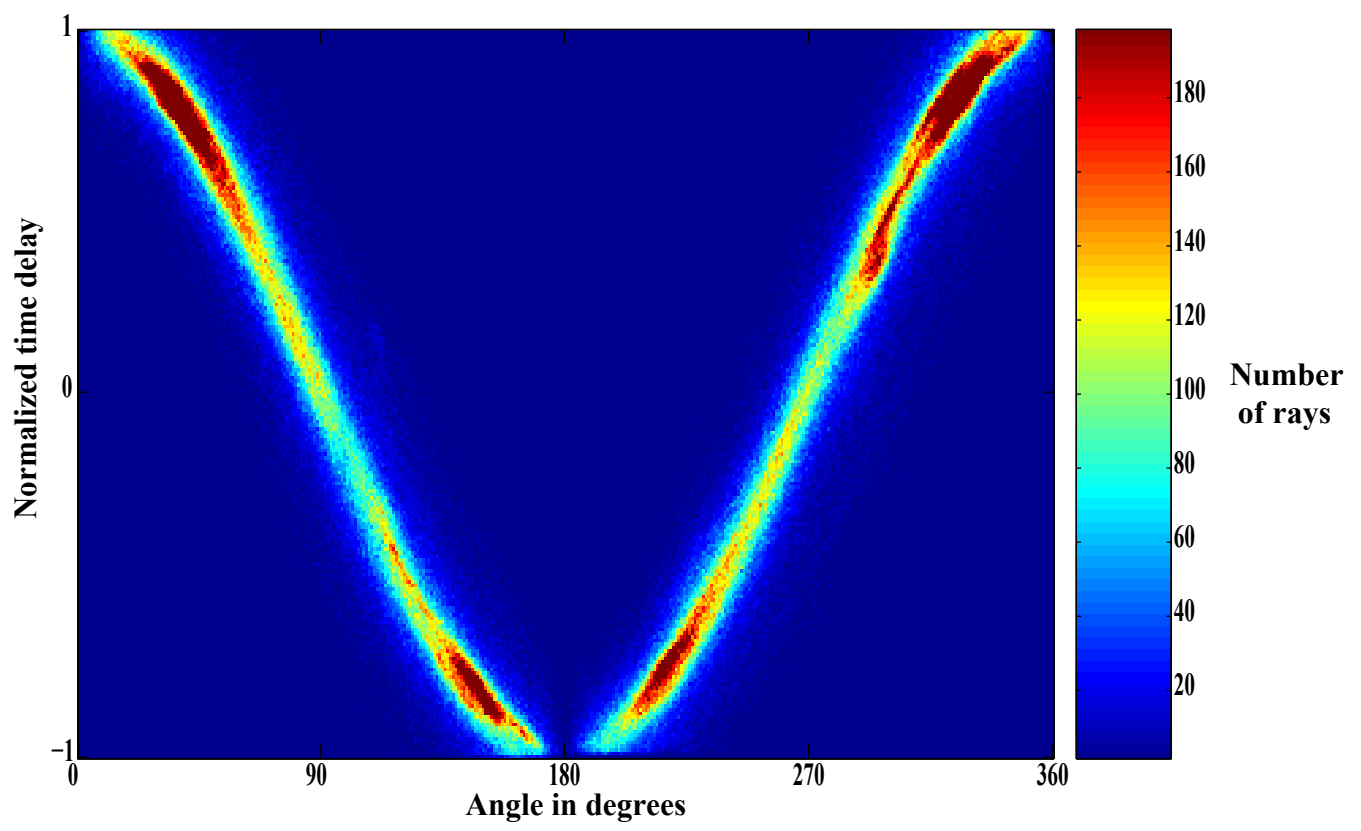
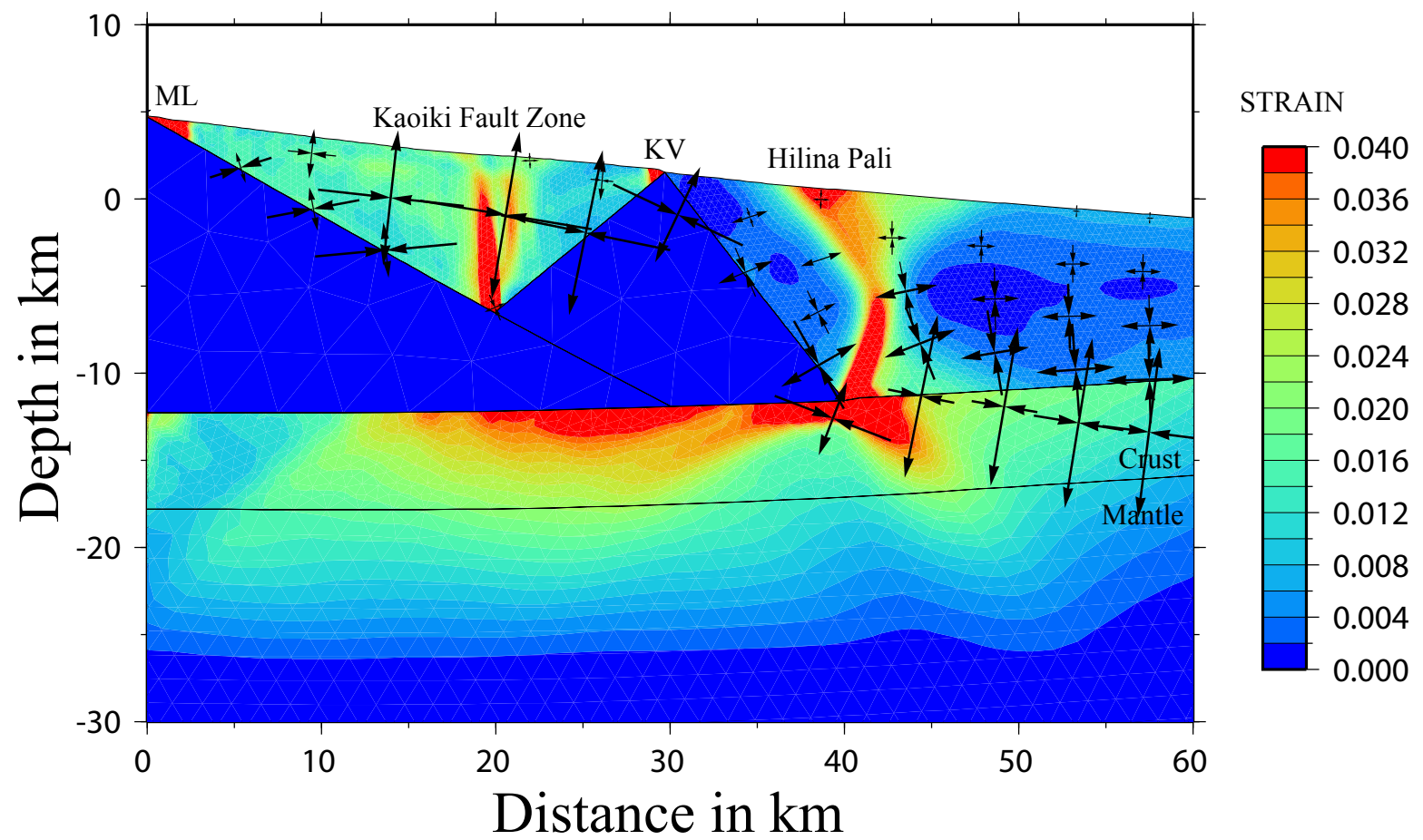**Figure 2b**

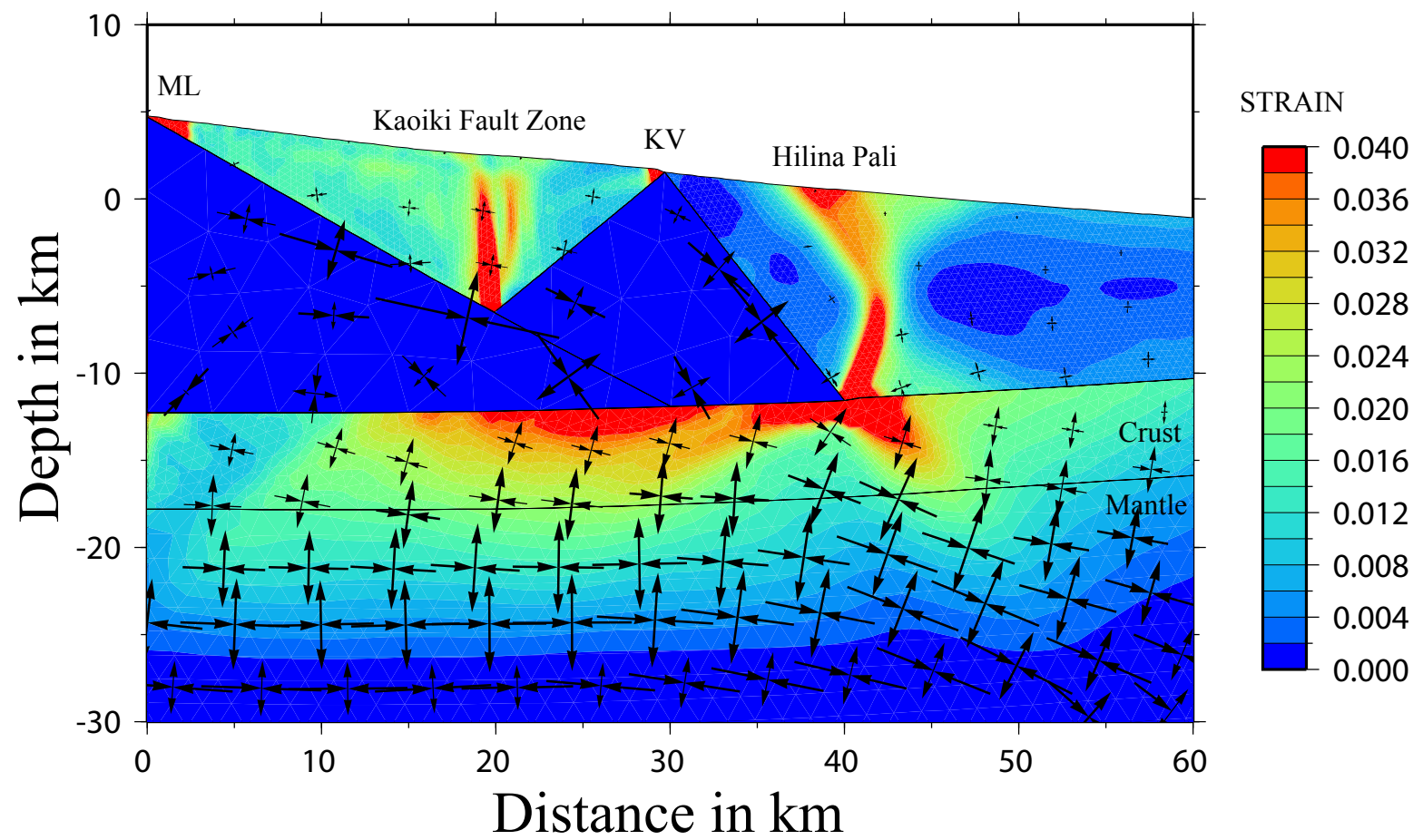**Figure 2c**

Figure 3a

Figure 3b

Figure 4a

Figure 4b

Figure SOM 1

Figure SOM2